

POISSON IMAGE DENOISING BASED ON FRACTIONAL-ORDER TOTAL VARIATION

MUJIBUR RAHMAN CHOWDHURY

Department of Mathematical Sciences, The University of Texas at Dallas
Richardson, TX 75080, USA

JUN ZHANG

Jiangxi Province Key Laboratory of Water Information Cooperative Sensing
and Intelligent Processing/College of Science, Nanchang Institute of Technology
Nanchang 330099, China

JING QIN

Department of Mathematics, University of Kentucky
Lexington, KY 40506, USA

YIFEI LOU*

Department of Mathematical Sciences, The University of Texas at Dallas
Richardson, TX 75080, USA

(Communicated by Martin Burger)

ABSTRACT. Poisson noise is an important type of electronic noise that is present in a variety of photon-limited imaging systems. Different from the Gaussian noise, Poisson noise depends on the image intensity, which makes image restoration very challenging. Moreover, complex geometry of images desires a regularization that is capable of preserving piecewise smoothness. In this paper, we propose a Poisson denoising model based on the fractional-order total variation (FOTV). The existence and uniqueness of a solution to the model are established. To solve the problem efficiently, we propose three numerical algorithms based on the Chambolle-Pock primal-dual method, a forward-backward splitting scheme, and the alternating direction method of multipliers (ADMM), each with guaranteed convergence. Various experimental results are provided to demonstrate the effectiveness and efficiency of our proposed methods over the state-of-the-art in Poisson denoising.

1. Introduction. In photon-counting devices such as positron emission tomography [54] and astronomical imaging [23], noise is inevitably dependent on the number of photons. Since the number of photons follows a Poisson distribution, this type of noise is often referred to as *Poisson noise*. In terms of image denoising, the smaller the peak value of an original image is, the noisier the image becomes when corrupted by Poisson noise. Based on the statistical property of the Poisson distribution and maximum likelihood estimation [17], Poisson denoising and restoration

2010 *Mathematics Subject Classification.* Primary: 65F22, 65Y04; Secondary: 52A41, 49N45.
Key words and phrases. Poisson noise, expectation-maximization, fractional-order total variation.

* Corresponding author: Yifei Lou.

models often adopt the following data fitting term

$$(1) \quad \min_u H(u) := \int_{\Omega} \left(u(x) - f(x) \log u(x) \right) dx,$$

where f is an observed (noisy) image, u is an image to be recovered, and Ω is a bounded open domain in \mathbb{R}^2 (typically rectangular for images).

Recently, many regularization techniques have been investigated for Poisson denoising, including Tikhonov regularization [51], total variation (TV) [44], and high-order TV [8]. In particular, the TV-based Poisson denoising model [24] can be expressed as

$$(2) \quad \min_u \int_{\Omega} \left(|\nabla u(x)| + \beta \left(u(x) - f(x) \log u(x) \right) \right) dx,$$

where β is a positive parameter. There are a number of efficient algorithms for solving the TV-regularized Poisson denoising model (2) such as an alternating extra-gradient method [2], an inexact iteratively reweighted approach [13], a primal-dual algorithm [58], a dual algorithm [47], an augmented Lagrangian method [18], and the split Bregman method [30, 59, 68]. In addition to denoising, other applications involving TV and Poisson noise include image decomposition [36], image deblurring [31, 48, 56, 66], and phase retrieval [9].

As one of the most popular regularizations, TV performs well on piecewise constant images for preserving edges while removing noises. However, it causes staircasing artifacts and the loss of image contrasts, latter of which is particularly obvious for piecewise smooth images [32]. To address these issues, some high-order regularizations for the Gaussian denoising problem have been introduced, including non-local total variation [21], TV combined with a fourth-order diffusive term [8], Euler's elastic models [15, 49, 50, 61], a mean curvature model [69], a total generalized variation (TGV) model [4, 55], a second-order TGV [26], and TGV together with sparsity and/or shearlets [19, 27, 40]. Specifically for the Poisson denoising, some high-order methods include PDE based models [62, 67], a hybrid regularization combining TV with a fourth-order variation [20], and TGV-based Poisson denoising model [29]. In particular, the Lysaker-Lundervold-Tai (LLT) model [32] was proposed to minimize an objective functional involving the Laplacian, thus leading to a fourth-order partial differential equation (PDE). Despite of its effective suppression of staircasing artifacts, the LLT method introduces speckle artifacts.

Different from other types of high-order TV, the fractional-order total variation (FOTV) uses the derivatives with order greater than or equal to one, leading to a compact discrete form and thereby bringing computational convenience. It has been empirically shown that FOTV is able to suppress both staircasing and speckle artifacts [1]. By taking the neighboring image intensities into account, FOTV can preserve local geometric characteristics. For example, FOTV can preserve textures [37, 38, 39] and image contrasts [60]. By extending the definition from a 2D domain to a graph, the FOTV regularization has been successfully applied to the electroencephalography (EEG) source imaging [28, 41, 42]. Other applications involving the FOTV regularization include image restoration from Gaussian noise [10, 14, 25, 33, 60], multiplicative noise removal [52, 53, 64], impulse noise removal [7], image decomposition [34], image reconstruction [65], and fluorescence microscopy image deconvolution [43].

Motivated by the success of FOTV in preserving image features and contrasts, we propose a Poisson denoising model based on FOTV to preserve high-order smoothness of an image. To the best of our knowledge, this is the first time that FOTV is considered for Poisson noise. The major contributions of the paper are three-fold:

- (1) We provide a rigorous discussion of the existence and uniqueness of the solution to the proposed model, based on the properties of the corresponding function space.
- (2) We derive three algorithms, which can shed lights on computational efficiency for such a nonlinear problem. Convergence guarantee of each proposed algorithm is also analyzed, which offers some guidance on parameter selection.
- (3) We conduct extensive experiments including a toy example and several natural images to demonstrate that our approach has superior performance over the state-of-the-art methods in Poisson denoising.

The rest of the paper is organized as follows. Section 2 provides both continuous and discrete formulations of the FOTV regularization together with analysis on existence and uniqueness. Three numerical schemes are detailed in Section 3 including the Chambolle-Pock's primal-dual (PD) method, a forward-backward splitting (FBS) scheme, and an alternating direction method of multiplier (ADMM). Experimental results on a synthetic image and five standard images are presented in Section 4 to illustrate the effectiveness and efficiency of our proposed methods. Finally, Section 5 concludes the paper.

2. Our proposed model. In this section, we first introduce the definition of FOTV and its related function space. Then we propose a variational model of FOTV-regularized Poisson denoising. Using the properties of FOTV, we can show that there uniquely exists a solution to our model. To ease the exposition of numerics, we provide discrete gradients and divergence for the implementations of FOTV.

2.1. Fractional-order total variation. Let $\mathcal{C}_0^\alpha(\Omega)$ with $\alpha > 0$ be the space of α -order continuously differentiable functions defined on Ω with compact support. The α -order total variation is then defined as

$$(3) \quad TV^\alpha(u) = \sup \left\{ \int_{\Omega} u \operatorname{div}^\alpha \Phi \, dx : \Phi = (\phi_1, \phi_2) \in (\mathcal{C}_0^\alpha(\Omega))^2, |\phi_i|_{L^\infty(\Omega)} \leq 1, i = 1, 2 \right\}.$$

Here the α -order divergence is given by

$$\operatorname{div}^\alpha \Phi = \frac{\partial^\alpha \phi_1}{\partial x^\alpha} + \frac{\partial^\alpha \phi_2}{\partial y^\alpha},$$

where $\frac{\partial^\alpha \phi_i}{\partial z^\alpha}$ with $z \in \{x, y\}$ is the α -order derivative of ϕ_i along the z -direction for $i = 1, 2$. Due to the convenience in numerical implementation, we adopt the Grünwald-Letnikov (GL) fractional-order derivative [63]. Based on the seminorm defined in (3), we define the space of functions with bounded α -order total variation, denoted by $BV^\alpha(\Omega) := \{u \in L^1(\Omega) : TV^\alpha(u) < \infty\}$. Similar to the space of functions with bounded variations, it can be shown that $BV^\alpha(\Omega)$ is a Banach space and any functional $J : BV^\alpha(\Omega) \rightarrow \mathbb{R}^+$ is lower semi-continuous [60].

2.2. FOTV Poisson denoising model. By incorporating the Poisson data fidelity term (1), we propose an FOTV-regularized Poisson denoising model

$$(4) \quad \min_{u \in BV^\alpha(\Omega)} TV^\alpha(u) + \beta \int_{\Omega} (u - f \log u) dx,$$

where $TV^\alpha(u)$ is defined in (3) and $\beta > 0$ is a weighting parameter to balance the regularization term and the data fitting. Theorem 2.1 establishes the existence and uniqueness of solutions to the proposed model (4).

Theorem 2.1. *Given $f > 0$ on Ω and $\beta > 0$, the problem (4) admits a unique solution in $BV^\alpha(\Omega)$.*

By using the fact that FOTV is convex, the proof is similar to [24, 29, 30], thus omitted.

2.3. Discrete fractional-order gradient and divergence. For $u \in BV^\alpha(\Omega)$, we discretize the image domain Ω as a rectangular grid $\{(x_i, y_j) : 1 \leq i \leq N, 1 \leq j \leq M\}$. Then an image can be represented as a matrix in the Euclidean space $\mathbb{R}^{N \times M}$, denoted as $u_{i,j} = u(x_i, y_j)$. Based on the GL fractional-order derivatives [63], the discrete fractional-order gradient is defined as

$$(5) \quad \nabla^\alpha u = [D_1^\alpha u, D_2^\alpha u],$$

where the discrete gradients $D_1^\alpha u, D_2^\alpha u \in \mathbb{R}^{N \times M}$ along the x -axis and the y -axis are given by

$$(6) \quad \begin{aligned} (D_1^\alpha u)_{i,j} &= \sum_{k=0}^{K-1} (-1)^k C_k^\alpha u_{i-k,j}, \\ (D_2^\alpha u)_{i,j} &= \sum_{k=0}^{K-1} (-1)^k C_k^\alpha u_{i,j-k}. \end{aligned}$$

Here K is the number of neighboring pixels that are used to compute the fractional-order derivative at each pixel. The coefficients $\{C_k^\alpha\}_{k=0}^{K-1}$ are given by $C_k^\alpha = \frac{\Gamma(\alpha+1)}{\Gamma(k+1)\Gamma(\alpha+1-k)}$ with the Gamma function $\Gamma(x)$. Then the discrete fractional-order total variation of $u \in \Omega$ is defined as

$$(7) \quad J(u) = \|\nabla^\alpha u\|_1 := \sum_{i,j} |(D_1^\alpha u)_{i,j}| + |(D_2^\alpha u)_{i,j}|.$$

Using the relation that $(\nabla^\alpha)^* = \overline{(-1)^\alpha} \operatorname{div}^\alpha$, the discrete fractional-order divergence $\operatorname{div}^\alpha \mathbf{p} \in \mathbb{R}^{N \times M}$ for $\mathbf{p} = (p^{(1)}, p^{(2)}) \in \mathbb{R}^{N \times M} \times \mathbb{R}^{N \times M}$ is given by [63]

$$(8) \quad (\operatorname{div}^\alpha \mathbf{p})_{i,j} = (-1)^\alpha \sum_{k=0}^{K-1} (-1)^k C_k^\alpha (p_{i+k,j}^{(1)} + p_{i,j+k}^{(2)}).$$

2.4. Connections to the existing models. For $\alpha = 1$ in (6), it is straightforward to have $C_0^1 = 1$, $C_1^1 = 1$ and $C_k^1 = 0$ for $k \geq 2$ and hence we have that

$$(9) \quad (D_1^1 u)_{i,j} = u_{i,j} - u_{i-1,j}, \quad (D_2^1 u)_{i,j} = u_{i,j} - u_{i,j-1},$$

which are the first-order backward differences along the coordinate axes. In this case, FOTV is reduced to the standard TV when backward difference is adopted as a discretization scheme.

When $\alpha = 2$ in (6), we have $C_0^2 = C_2^2 = 1$, $C_1^2 = 2$, and $C_k^2 = 0$ for $k \geq 3$, which implies that

$$(10) \quad (D_1^2 u)_{i,j} = \sum_{k=0}^2 (-1)^k C_k^2 u_{i-k,j} = u_{i,j} - 2u_{i-1,j} + u_{i-2,j}.$$

Similarly, $(D_2^2 u)_{i,j} = u_{i,j} - 2u_{i,j-1} + u_{i,j-2}$. As a consequence, FOTV with $\alpha = 2$ can be expressed by $\int_{\Omega} (|u_{xx}| + |u_{yy}|) dz$, where u_{xx} and u_{yy} are discretized by

$$(11) \quad \begin{aligned} (u_{xx})_{i,j} &= u_{i+1,j} - 2u_{i,j} + u_{i-1,j}, \\ (u_{yy})_{i,j} &= u_{i,j+1} - 2u_{i,j} + u_{i,j-1}. \end{aligned}$$

This is equivalent to the LLT model [32]. In summary, FOTV is a general regularization framework including TV and LLT as its special case for $\alpha = 1$ and $\alpha = 2$, respectively.

3. Algorithms. For the purpose of implementation, we consider a discretized version of the Poisson denoising model (4) as follows,

$$(12) \quad \min_{u \in \mathbb{R}^{N \times M}} \|\nabla^{\alpha} u\|_1 + \beta \langle u - f \log u, \mathbf{1}_{\Omega} \rangle,$$

where $\mathbf{1}_{\Omega}$ denotes the indicator function on a discrete grid of the image domain Ω . We propose three efficient numerical algorithms based on three popular optimization methods, i.e., PD, FBS and ADMM. By discussing various optimization schemes, we can select the one with the optimal computational efficiency. More importantly, we can provide some rule of thumb regarding the optimal scheme for such nonlinear optimization problem.

3.1. Primal-dual algorithm. We rewrite the proposed model (12) as a minimax problem in order to apply the Chambolle-Pock primal-dual (PD) method [6]. It leads to two subproblems, each of which can be solved efficiently. The convergence of the scheme can be guaranteed as discussed in [6].

By letting

$$Au = \nabla^{\alpha} u, \quad F(Au) = \|\nabla^{\alpha} u\|_1, \quad H(u) = \beta \langle u - f \log u, \mathbf{1}_{\Omega} \rangle,$$

we express the proposed model (12) in the following form,

$$(13) \quad \min_u F(Au) + H(u).$$

It follows from the property of convex conjugate F^* that the convex conjugate function of F is given by

$$(14) \quad F^*(\mathbf{p}) = \begin{cases} 0, & \text{if } \|\mathbf{p}\|_{\infty} \leq 1; \\ +\infty, & \text{otherwise.} \end{cases}$$

We can then rewrite (13) as a minimax form

$$(15) \quad \min_u \max_{\mathbf{p}} \langle Au, \mathbf{p} \rangle - F^*(\mathbf{p}) + H(u).$$

Directly applying the Chambolle-Pock algorithm [6] for the minimax problem (15) yields the following iterative scheme,

$$(16) \quad \begin{cases} \mathbf{p}^{k+1} = \underset{\mathbf{p}}{\operatorname{argmax}} \langle \nabla^\alpha \bar{u}^k, \mathbf{p} \rangle - F^*(\mathbf{p}) - \frac{\|\mathbf{p} - \mathbf{p}^k\|_2^2}{2\sigma} \\ u^{k+1} = \underset{u}{\operatorname{argmin}} \langle u, \overline{(-1)^\alpha \operatorname{div}^\alpha \mathbf{p}^{k+1}} \rangle + H(u) + \frac{\|u - u^k\|_2^2}{2\tau} \\ \bar{u}^{k+1} = u^{k+1} + \theta(u^{k+1} - u^k), \end{cases}$$

where σ , τ and θ are positive tuning parameters. Note that the u -subproblem is derived due to the relationship between the two operators ∇^α and $\operatorname{div}^\alpha$, i.e.,

$$\langle \nabla^\alpha u, \mathbf{p} \rangle = \langle u, \overline{(-1)^\alpha \operatorname{div}^\alpha \mathbf{p}} \rangle.$$

In what follows, we describe the respective closed-form solutions for the two subproblems in (16). Specifically, the \mathbf{p} -subproblem is equivalent to

$$(17) \quad \mathbf{p}^{k+1} = \underset{\mathbf{p}}{\operatorname{argmin}} F^*(\mathbf{p}) + \frac{\|\mathbf{p} - (\mathbf{p}^k + \sigma \nabla^\alpha \bar{u}^k)\|_2^2}{2\sigma}.$$

It has a closed-form solution, given by

$$(18) \quad \mathbf{p}_{i,j}^{k+1} = \begin{cases} \tilde{\mathbf{p}}_{i,j}, & |\tilde{\mathbf{p}}_{i,j}| \leq 1, \\ \frac{\tilde{\mathbf{p}}_{i,j}}{|\tilde{\mathbf{p}}_{i,j}|}, & \text{otherwise,} \end{cases}$$

for $\tilde{\mathbf{p}} = \mathbf{p}^k + \sigma \nabla^\alpha u^k$. As for the u -subproblem, the solution can be obtained by solving the corresponding Euler-Lagrange equation of the form

$$\frac{1}{\tau} u^2 + (\alpha - \tilde{u})u - \alpha f \tau = 0,$$

where $\tilde{u} = u^k - \tau \overline{(-1)^\alpha \operatorname{div}^\alpha \mathbf{p}^{k+1}}$. By using the quadratic formula, we get a non-negative solution of u , i.e.,

$$(19) \quad u^{k+1} = \frac{\tilde{u} - \beta\tau}{2} + \sqrt{\left(\frac{\tilde{u} - \beta\tau}{2}\right)^2 + \beta\tau f}.$$

We summarize the FOTV regularized Poisson denoising via PD in Algorithm 1. The convergence of this algorithm is guaranteed by the following theorem, whose proof is presented in [6].

Theorem 3.1. *Let $L = \|\nabla^\alpha\|$ and assume the problem (15) has a saddle point. Choose $\theta = 1$, $\tau\sigma L^2 < 1$, and let $(\mathbf{p}^k, u^k, \bar{u}^k)$ be defined by (16). Then there exists a saddle point (x^*, y^*) such that $x^n \rightarrow x^*$ and $y^n \rightarrow y^*$ as $n \rightarrow \infty$.*

Remark. We seek an upper bound of L that enables the convergence of the proposed PD algorithm as well as provides guidance on choosing appropriate values of

Algorithm 1: FOTV Poisson denoising via PD.

Input: the observed image f
Set parameters: $\alpha, \beta, \sigma, \tau, \epsilon$
Initialization: $\mathbf{p}^0 = \mathbf{0}, u^0 = f$
while $\frac{\|u^{k+1} - u^k\|}{\|u^k\|} < \epsilon$ **do**
 $\mathbf{p}^{k+1} = \frac{\tilde{\mathbf{p}}}{\max(1, |\tilde{\mathbf{p}}|)}$, where $\tilde{\mathbf{p}} = \mathbf{p}^k + \sigma \nabla^\alpha u^k$
 $u^{k+1} = \frac{\tilde{u} - \beta\tau}{2} + \sqrt{\left(\frac{\tilde{u} - \beta\tau}{2}\right)^2 + \beta\tau f}$, where $\tilde{u} = u^k - \tau(-1)^\alpha \operatorname{div}^\alpha \mathbf{p}^{k+1}$
 $\bar{u}^{k+1} = u^{k+1} + \theta(u^{k+1} - u^k)$
 $k = k + 1$
end
Output: u

the parameters τ and σ . For this purpose, we estimate

$$\begin{aligned} \|\nabla^\alpha u\|^2 &= \sum_{i,j} \left(\sum_{k=0}^{K-1} (-1)^\alpha C_k^\alpha u_{i-k,j} \right)^2 + \sum_{i,j} \left(\sum_{k=0}^{K-1} (-1)^\alpha C_k^\alpha u_{i,j-k} \right)^2 \\ &\leq \sum_{i,j} \left(\sum_{k=0}^{K-1} |C_k^\alpha|^2 \right) \left(\sum_{k=0}^{K-1} u_{i-k,j}^2 \right) + \sum_{i,j} \left(\sum_{k=0}^{K-1} |C_k^\alpha|^2 \right) \left(\sum_{k=0}^{K-1} u_{i,j-k}^2 \right) \\ &= \left(\sum_{k=0}^{K-1} |C_k^\alpha|^2 \right) \sum_{i,j} \sum_{k=0}^{K-1} (u_{i-k,j}^2 + u_{i,j-k}^2) = 2K \left(\sum_{k=0}^{K-1} |C_k^\alpha|^2 \right) \sum_{i,j} u_{i,j}^2 \end{aligned}$$

Therefore, $L^2 \leq 2K \sum_{k=0}^{K-1} |C_k^\alpha|^2$. For the special case of TV, i.e., $\alpha = 1, K = 2$, we have $L^2 \leq 8$, which is consistent in [5]. Following discussion in Section 2.4, FOTV with $\alpha = 2$ has fewer terms than anisotropic LLT and hence the upper bound of L with $\alpha = 2, K = 3$ ($L^2 \leq 36$) is smaller than that of LLT ($L^2 \leq 64$ in [11]).

3.2. Forward-backward splitting algorithm. Motivated by the works [46, 47], we consider the first-order optimality condition of (12), i.e.,

$$(20) \quad v + \beta \left(\mathbf{1}_\Omega - \frac{f}{u} \right) = 0,$$

where $v \in \partial J(u)$ is a subderivative of the functional J at u . At the k -th iteration, we adopt the following discretization scheme

$$(21) \quad v^{k+1} + \beta \left(\frac{u^{k+1}}{u^k} - \frac{f}{u^k} \right) = 0,$$

where the constant term $\mathbf{1}_\Omega$ is approximated by $\frac{u^{k+1}}{u^k}$ and this method is referred to as the *forward-backward splitting* (FBS) method. It follows from the optimality condition (21) that u^{k+1} is an optimal solution of the problem, i.e.,

$$(22) \quad u^{k+1} = \arg \min_u J(u) + \frac{\beta}{2} \left\langle \frac{(u-f)^2}{u^k}, \mathbf{1}_\Omega \right\rangle.$$

We want to point out that the convergence of the FBS scheme (21) can be proved in a similar way as in [46].

We then describe how to solve for the subproblem of (22) by introducing an auxiliary variable \mathbf{z} in such a way that (22) is equivalent to

$$(23) \quad \min_{u, \mathbf{z}} \|\mathbf{z}\|_1 + \frac{\beta}{2} \left\langle \frac{(u-f)^2}{u^k}, \mathbf{1}_\Omega \right\rangle, \quad \text{s.t.} \quad \mathbf{z} = \nabla^\alpha u.$$

To efficiently handle the L_1 term of this model, we choose a dual formulation [5]. Specifically, we construct the corresponding Lagrangian functional

$$\mathcal{L}(u, \mathbf{z}; \boldsymbol{\lambda}) = \|\mathbf{z}\|_1 + \frac{\beta}{2} \left\langle \frac{(u-f)^2}{u^k}, \mathbf{1}_\Omega \right\rangle + \langle \boldsymbol{\lambda}, \nabla^\alpha u - \mathbf{z} \rangle.$$

Since \mathcal{L} is separable with respect to u and \mathbf{z} , the dual functional is given by

$$(24) \quad \begin{aligned} q(\boldsymbol{\lambda}) &= \inf_{u, \mathbf{z}} \mathcal{L}(u, \mathbf{z}; \boldsymbol{\lambda}) \\ &= \inf_u \left(\frac{\beta}{2} \left\langle \frac{(u-f)^2}{u^k}, \mathbf{1}_\Omega \right\rangle + \langle (\nabla^\alpha)^* \boldsymbol{\lambda}, u \rangle \right) + \inf_{\mathbf{z}} (\|\mathbf{z}\|_1 - \langle \boldsymbol{\lambda}, \mathbf{z} \rangle). \end{aligned}$$

The minimizer u of (24) can be expressed as

$$(25) \quad u = f - \frac{(\nabla^\alpha)^* \boldsymbol{\lambda}}{\beta} u^k.$$

By the dual norm of L_1 -norm, we can get a closed-form solution of \mathbf{z} using a characteristic function

$$\inf_{\mathbf{z}} (\|\mathbf{z}\|_1 - \langle \boldsymbol{\lambda}, \mathbf{z} \rangle) = \chi_S(\boldsymbol{\lambda}) = \begin{cases} 0, & \boldsymbol{\lambda} \in S; \\ +\infty, & \text{otherwise,} \end{cases}$$

where $S = \{\boldsymbol{\lambda} \mid \|\boldsymbol{\lambda}\|_\infty \leq 1\}$. Therefore, the dual problem of (22) becomes

$$(26) \quad \begin{aligned} \max_{\boldsymbol{\lambda}} q(\boldsymbol{\lambda}) &= -\min_{\boldsymbol{\lambda}} \frac{u^k}{2\beta} \langle ((\nabla^\alpha)^* \boldsymbol{\lambda})^2, \mathbf{1}_\Omega \rangle - \langle (\nabla^\alpha)^* \boldsymbol{\lambda}, f \rangle + \chi_S(\boldsymbol{\lambda}) \\ &= -\min_{\|\boldsymbol{\lambda}\|_\infty \leq 1} \frac{u^k}{2\beta} \left\| (\nabla^\alpha)^* \boldsymbol{\lambda} - \frac{\beta f}{u^k} \right\|_2^2. \end{aligned}$$

Define

$$\boldsymbol{\theta}(\boldsymbol{\lambda}; u^k) = \left(\nabla^\alpha \left((\nabla^\alpha)^* \boldsymbol{\lambda} - \frac{\beta f}{u^k} \right) \right),$$

whose (i, j) -th entry is denoted by $\boldsymbol{\theta}(\boldsymbol{\lambda}; u^k)_{i,j}$. Then the Karush-Kuhn-Tucker conditions yield the existence of a Lagrange multiplier $\gamma_{i,j} \geq 0$, associated to each component $\boldsymbol{\lambda}_{i,j}$. For each index pair (i, j) , we have

$$-\boldsymbol{\theta}(\boldsymbol{\lambda}; u^k)_{i,j} + \gamma_{i,j} \boldsymbol{\lambda}_{i,j} = 0.$$

If $|\boldsymbol{\lambda}_{i,j}| = 1$, then $\gamma_{i,j} > 0$. If $|\boldsymbol{\lambda}_{i,j}| < 1$, then $\gamma_{i,j} = 0$ and

$$\boldsymbol{\theta}(\boldsymbol{\lambda}; u^k)_{i,j} = 0.$$

In either case, we have

$$\gamma_{i,j} = |\boldsymbol{\theta}(\boldsymbol{\lambda}; u^k)_{i,j}|.$$

Therefore, we consider to solve for $\boldsymbol{\lambda}_{i,j}$ from the following equation

$$(27) \quad -\boldsymbol{\theta}(\boldsymbol{\lambda}; u^k)_{i,j} + |\boldsymbol{\theta}(\boldsymbol{\lambda}; u^k)_{i,j}| \boldsymbol{\lambda}_{i,j} = 0.$$

via the semi-implicit gradient descent algorithm. More specifically, given a step size $\tau > 0$, the l -th iteration goes as follows,

$$(28) \quad \boldsymbol{\lambda}_{i,j}^{l+1} = \boldsymbol{\lambda}_{i,j}^l + \tau \left(\boldsymbol{\theta}(\boldsymbol{\lambda}^l; u^k)_{i,j} - |\boldsymbol{\theta}(\boldsymbol{\lambda}^l; u^k)_{i,j}| \boldsymbol{\lambda}_{i,j}^{l+1} \right),$$

Algorithm 2: FOTV Poisson denoising via FBS.

Input: f
Set parameters: $\alpha, \beta, \tau, \epsilon$ and maximum inner iteration number N_{in}
Initialization: $\lambda^0 = \mathbf{0}, u^0 = f$
while $\frac{\|u^{k+1} - u^k\|}{\|u^k\|} < \epsilon$ **do**
 for $l = 1, \dots, N_{in}$ **do**
 | $\lambda^{k,l+1}$ is updated by (29)
 end
 $\lambda^{k+1} = \lambda^{k, N_{in}}$
 $u^{k+1} = f - \frac{u^k}{\beta} (\nabla^\alpha)^* \lambda^{k+1}$
 $k = k + 1$
end
Output: u

which is equivalent to

$$(29) \quad \lambda_{i,j}^{l+1} = \frac{\lambda_{i,j}^l + \tau \theta(\lambda^l; u^k)_{i,j}}{1 + \tau |\theta(\lambda^l; u^k)_{i,j}|}.$$

Once λ is obtained, the update for u is given by (25). The entire FBS scheme (22) with a dual algorithm for the subproblem is summarized in Algorithm 2.

3.3. Augmented Lagrangian method. We adopt the alternating direction method of multipliers (ADMM) [3] to solve the proposed model (12). In particular, we introduce an auxiliary variable \mathbf{z} to reformulate (12) as,

$$(30) \quad \min_{u, \mathbf{z}} \|\mathbf{z}\|_1 + \beta \langle u - f \log u, \mathbf{1}_\Omega \rangle \quad \text{s.t.} \quad \mathbf{z} = \nabla^\alpha u.$$

The augmented Lagrangian functional corresponding to (30) is

$$(31) \quad \mathcal{L}(u, \mathbf{z}; \lambda) = \|\mathbf{z}\|_1 + \langle \lambda, \mathbf{z} - \nabla^\alpha u \rangle + \frac{\mu}{2} \|\mathbf{z} - \nabla^\alpha u\|_2^2 + \beta \langle u - f \log u, \mathbf{1}_\Omega \rangle,$$

where λ is Lagrangian multiplier and μ is a positive parameter. Then ADMM yields the following algorithm,

$$(32) \quad \begin{cases} u^{k+1} = \underset{u}{\operatorname{argmin}} \mathcal{L}(u, \mathbf{z}^k; \lambda^k), \\ \mathbf{z}^{k+1} = \underset{\mathbf{z}}{\operatorname{argmin}} \mathcal{L}(u^{k+1}, \mathbf{z}; \lambda^k), \\ \lambda^{k+1} = \lambda^k + \mu(\mathbf{z}^{k+1} - \nabla^\alpha u^{k+1}). \end{cases}$$

To solve the u -subproblem in (32), we consider the Euler-Lagrange equation of (31) with respect to u , which has the form

$$(33) \quad -(\nabla^\alpha)^* \lambda^k - \mu(\nabla^\alpha)^*(\mathbf{z}^k - \nabla^\alpha u) + \beta(u - f)/u = 0.$$

In order to efficiently solve the nonlinear equation (33), we replace u in the denominator by the previous iteration u^k and solve for u^{k+1} by using the fast Fourier transform (FFT) with periodic boundary conditions. More specifically, u^{k+1} is given by

$$(34) \quad u^{k+1} = \mathcal{F}^{-1} \left(\frac{\mathcal{F}[(\beta f + u^k \circ (\nabla^\alpha)^* \lambda^k)/\mu + u^k \circ (\nabla^\alpha)^* \mathbf{z}^k]}{\beta/\mu + u^k \circ \mathcal{F}((\nabla^\alpha)^*) \mathcal{F}(\nabla^\alpha)} \right),$$

Algorithm 3: FOTV Poisson denoising via ADMM

Input: f
 Set parameters: $\alpha, \beta, \mu, \epsilon$
 Initialization: $\mathbf{z}^0 = \mathbf{0}, \boldsymbol{\lambda}^0 = \mathbf{0}, u^0 = f$
while $\frac{\|u^{k+1} - u^k\|}{\|u^k\|} < \epsilon$ **do**
 $u^{k+1} = \mathcal{F}^{-1} \left(\frac{\mathcal{F}[(\beta f + u^k \circ (\nabla^\alpha)^* \boldsymbol{\lambda}^k) / \mu + u^k \circ (\nabla^\alpha)^* \mathbf{z}^k]}{\beta / \mu + u^k \circ \mathcal{F}((\nabla^\alpha)^*) \mathcal{F}(\nabla^\alpha)} \right)$
 $\mathbf{z}^{k+1} = \text{shrink}(\nabla^\alpha u^{k+1} - \frac{\boldsymbol{\lambda}^k}{\mu}, \frac{1}{\mu})$
 $\boldsymbol{\lambda}^{k+1} = \boldsymbol{\lambda}^k + \mu(\mathbf{z}^{k+1} - \nabla^\alpha u^{k+1})$
 $k = k + 1$
end
 Output: u

where \mathcal{F} is the Fourier transform and \circ is the component-wise multiplication. Note that the update in (34) is an approximation to the solution of the nonlinear problem (33). We can iterate (34) for a few times in order to get a better solution, but empirical evidence shows that one iteration is sufficient to give a reasonable solution. In addition, there is a closed-form solution for the \mathbf{z} -subproblem given by

$$(35) \quad \mathbf{z}^{k+1} = \text{shrink}(\nabla^\alpha u^{k+1} - \frac{\boldsymbol{\lambda}^k}{\mu}, \frac{1}{\mu}),$$

where $\text{shrink}(s, \gamma) := \text{sgn}(s) \max\{|s| - \gamma, 0\}$. The ADMM algorithm for solving the FOTV-based Poisson denoising model is summarized in Algorithm 3. Convergence of ADMM for a general convex problem was proven by Eckstein and Bertsekas [16], which is described as follows.

Theorem 3.2 (Eckstein and Bertsekas [16]). *Consider a convex problem of the form*

$$(36) \quad \min_u F(u) + G(u),$$

where F, G are proper convex functionals. Suppose we are given $\mu > 0$ and $\{\mu_k\}_{k=0}^\infty \subseteq [0, \infty)$ and $\{\rho_k\}_{k=0}^\infty \subseteq [0, \infty)$ be two sequences such that $\sum_{k=0}^\infty \mu_k < \infty$ and $\sum_{k=0}^\infty \rho_k < \infty$. Suppose three sequences $\{u^k\}$, $\{\mathbf{z}^k\}$ and $\{\boldsymbol{\lambda}^k\}$ conform to

$$(37) \quad \begin{aligned} \|u^{k+1} - \underset{u}{\text{argmin}} \mathcal{L}(u, \mathbf{p}^k; \boldsymbol{\lambda}^k) &\leq \mu_k, \\ \|\mathbf{z}^{k+1} - \underset{\mathbf{z}}{\text{argmin}} \mathcal{L}(u^{k+1}, \mathbf{z}; \boldsymbol{\lambda}^k) &\leq \rho_k, \\ \boldsymbol{\lambda}^{k+1} &= \boldsymbol{\lambda}^k + \mu(\mathbf{z}^{k+1} - \nabla^\alpha u^{k+1}), \end{aligned}$$

for all k . Then if (36) has a solution u^* , the sequence $\{u^k\}$ converges to u^* . If (36) has no solution, then at least one of the sequences $\{\mathbf{z}^k\}$ or $\{\boldsymbol{\lambda}^k\}$ is unbounded.

Remark. It is straightforward to see that the functionals F, G in our problem (12) are proper and convex. The existence of solutions is guaranteed by Theorem 2.1. If u and \mathbf{z} subproblems can be solved with sufficient accuracy, the convergence of Algorithm 3 is guaranteed by Theorem 3.2.

4. Numerical experiments. In this section, we present extensive numerical results of the proposed Poisson denoising method, in comparison with some state-of-the-art methods. Since Poisson noise depends on the pixel intensity, the noise level can be controlled by the peak intensity of the original image. In order to examine

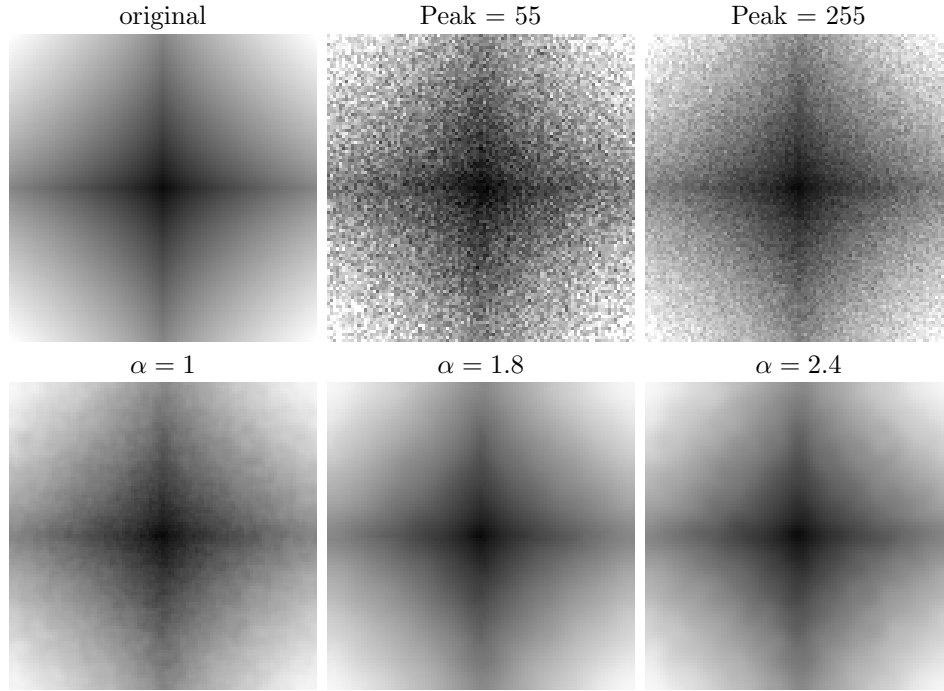


FIGURE 1. A synthetic example. Top: the synthetic ground-truth image and two noisy images with peak values 55 and 255, respectively. Bottom: FOTV Poisson denoising results (via Algorithm 3) with the respective fractional order 1, 1.8, and 2.4 for the case with peak value 255.

the performance of various Poisson denoising methods for different noise levels, we scale the original image with a pre-set peak value, before adding Poisson noise. Specifically, we consider three peak values: 55, 155, 255. The larger the peak value is, the less noisy the observed image becomes, see Figure. 1.

The test images include a synthetic image and five standard images, i.e., Camera-man, Penguin, Train, Mandrill, and Barbara, all of which are widely used in the image processing literature. The synthetic image is constructed by $u(x, y) = |x|^a + |y|^a$ with $a = 0.8$ and the image domain $\Omega = [-50, 50] \times [-50, 50]$. By the theory of kernel functions of FOTV [60], the optimal fractional order for denoising this synthetic image is $\alpha = a + 1 = 1.8$. In Figure. 1, we show this ground-truth image together with two noisy images of peak values at 55 and 255, respectively. One can see that the image with peak 55 is more noisy compared the one with peak 255. We present the denoising results at peak 255 using different fractional orders $\alpha = 1, 1.8$, and 2.4. The bottom row of Figure. 1 illustrates staircasing artifacts when $\alpha = 1$ in FOTV (i.e., TV) and the over-smoothing phenomenon when $\alpha = 2.4$.

Next we compare three minimizing algorithms for the proposed FOTV model, followed by comparison with some popular Poisson denoising methods, including NPTTool [22], NL-PCA [45], and BM3D [35]. NPTTool [22] is a MATLAB toolbox for the nonnegative image restoration with Newton projection methods, among which we use the total variation model. NL-PCA [45] is based on the idea of nonlocal

patches together with principal component analysis (PCA) for Poisson noise reduction. BM3D [35] for Poisson denoising involves the Anscombe transformation that converts Poisson noise into Gaussian noise, followed by the Gaussian denoising using BM3D [12].

We use the peak-signal-to-noise-ratio (PSNR) and structural-similarity (SSIM) index [57] for quantitative comparison. The PSNR is defined as

$$(38) \quad \text{PSNR}(X, Y) = 10 \log_{10} \frac{R^2}{\frac{1}{MN} \sum_{i=1}^M \sum_{j=1}^N (X_{i,j} - Y_{i,j})^2},$$

where R is the maximum peak value of the original image X and Y is the restored image. As for SSIM, we define the *local* similarity index computed on two small patches x and y ,

$$(39) \quad \text{ssim}(x, y) = \frac{(2\mu_x\mu_y + c_1)(2\sigma_{xy} + c_2)}{(\mu_x^2 + \mu_y^2 + c_1)(\sigma_x^2 + \sigma_y^2 + c_2)},$$

where $\mu_x/\sigma_x^2, \mu_y/\sigma_y^2$ are the average/variance of x, y , σ_{xy} is the covariance of x, y , and two positive parameters c_1, c_2 are set to avoid the denominator being zero. The overall SSIM is the mean of local similarity indexes, i.e.,

$$(40) \quad \text{SSIM}(X, Y) = \frac{1}{P} \sum_{i=1}^P \text{ssim}(x_i, y_i),$$

where x_i, y_i are the corresponding patches indexed by i and P is the number of patches. All numerical experiments are performed under Windows 7 and MATLAB R2017b running on a desktop with Intel(R) Core(TM) i7-4790 CPU @ 3.60GHz.

4.1. Comparison of proposed algorithms. We compare the efficiency of the three proposed algorithms, i.e., Algorithms 1-3, by minimizing the same objective function (12). In all experiments, the stop criterion is $\frac{\|u^{k+1} - u^k\|}{\|u^k\|} < 1e^{-5}$. For the synthetic image, we fix $\alpha = 1.8$ (ground-truth value), $K = 20$, and $\beta = 7$. We optimize other algorithmic parameters for each algorithm when plotting the energy and PSNR values with respect to time (in seconds). The results are provided in Figure 2, which shows that Algorithm 2 is the fastest algorithm to minimize the energy, but Algorithm 1 achieves the largest PSNR. Another example using Barbara image at peak 55 is also included in Figure 2, where we set $\alpha = 1.6$, $K = 20$ and $\beta = 12$. We observe that Algorithm 3 achieves the best results in terms of PSNR. As ADMM involves the least number of parameters compared to the other two algorithms, we will use it (Algorithm 3) for the rest of experiments. All the plots in Figure 2 numerically demonstrate the convergence of each algorithm.

In Figure 3, we illustrate how the fractional order α affects the image restoration. For each order in FOTV, we choose the best combination of parameters from the parameter sets of $\beta \in \{0.1, 1, 7, 10\}$ and $\mu \in \{10^{-5}, 10^{-4}, 10^{-3}, 2 \times 10^{-3}\}$. We then plot the largest PSNR as a function of fractional order for two peak levels 55 and 255. For the synthetic image, when peak is 255, the optimal order indeed occurs at the theoretical value $\alpha = 1.8$. However, it is not the case for peak value 55. This phenomenon occurs due to the presence of the truncation error when we approximate the fractional order derivative by only taking K adjacent pixels into consideration. In other words, when the noise level is high, we could increase the accuracy in discretization of the fractional order derivatives. We also include the PSNR value versus fractional order for the Barbara image in Figure 3, which

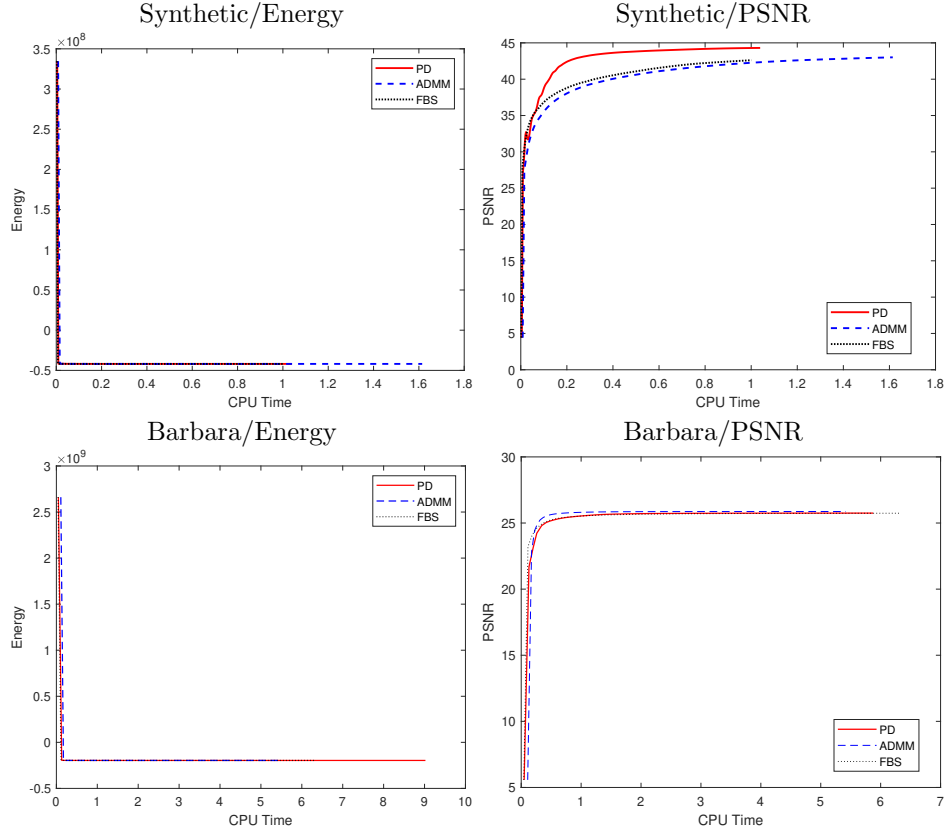


FIGURE 2. Algorithmic comparison in terms of energy (left) and PSNR (right) by denoising the noisy synthetic image with peak value of 255 (top) and the Barbara image with peak value of 55 (bottom).

shows advantages of fractional order derivatives over integer order ones. However, with complicated image contents, natural images usually have less obvious denoising improvements by using FOTV compared to synthetic ones, e.g., 5 db PSNR gain for the synthetic image versus 0.5 db for the Barbara image when comparing the optimal fractional order and the standard TV ($\alpha = 1$).

4.2. Comparison with various Poisson denoising methods. We compare the proposed Algorithm 3 with other state-of-the-art methods in Poisson denoising. Here is how we tune the parameters for each method. For our algorithm (ADMM), we choose the best combination of $\alpha \in \{1, 1.6, 2.3, 2.6\}$, $\beta \in \{6, 8, 12, 15, 20, 35, 58\}$, and $\mu \in \{10^{-5}, 5 \times 10^{-5}, 10^{-4}, 2 \times 10^{-4}, 3 \times 10^{-4}, 4 \times 10^{-4}, 5 \times 10^{-4}, 10^{-3}, 10^{-3}, 2 \times 10^{-3}, 3 \times 10^{-3}\}$. There is only a parameter for NPTTool, which is selected among $\eta \in \{8 \times 10^{-5}, 9 \times 10^{-5}, 10^{-4}, 2 \times 10^{-4}, 3 \times 10^{-4}, 5 \times 10^{-4}, 7 \times 10^{-4}\}$. The two parameters for NLPCA are number of clusters and patch width, which are chosen among the sets of $\{15, 46, 55, 59, 68, 73, 80, 82, 85, 89\}$ and $\{2, 3, 4, 5, 6, 8\}$, respectively.

We provide both PSNR and SSIM values in Table 1, which shows that the proposed approach achieves the best performance in most cases. Note that NPTTool

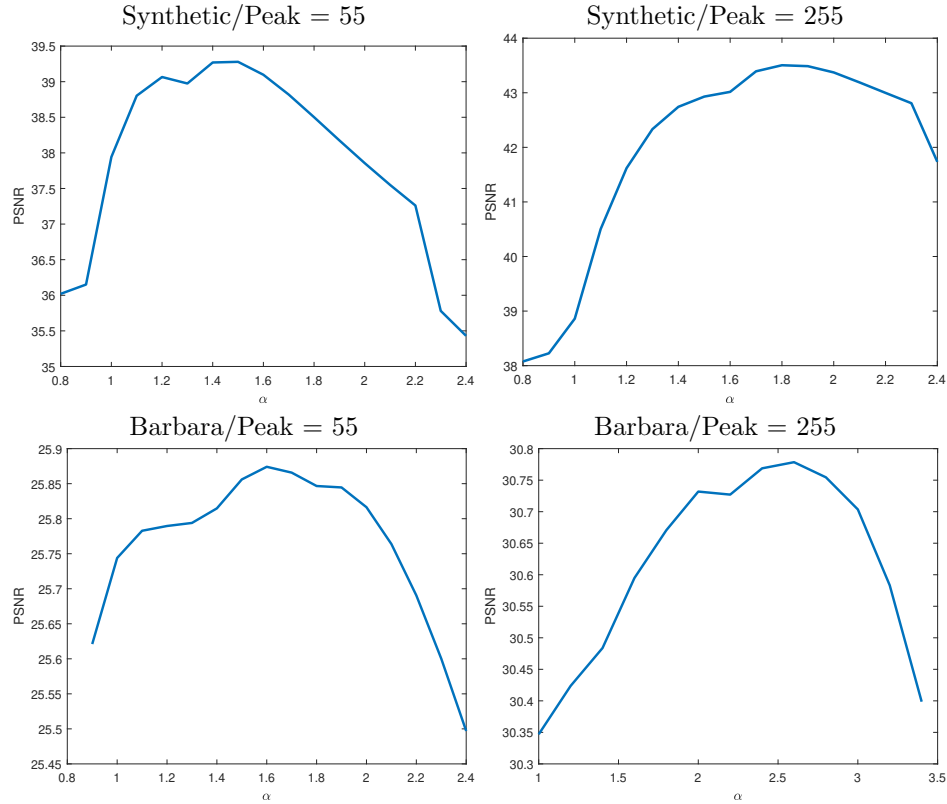


FIGURE 3. PSNR versus fractional orders for the synthetic image (top) and Barbara image (bottom) with peak values at 55 (left) and 255 (right).

is a TV-regularized denoising method and NL-PCA/BM3D are designed for texture images. Although BM3D works well on the Barbara image, it yields the worst restoration performance on the Mandril image. Since both the Barbara and Mandril images have rich textures, it indicates that BM3D is not robust to textures. The computational times for these methods are provided in Table 2.

We show some visual results of Poisson denoising in Figures 4-7, each with a zoom-in patch and the corresponding PSNR/SSIM values. In particular, Figures 4-5 illustrate staircasing artifacts of NPTTool and oversmoothing artifacts of BM3D. Oversmoothing is very obvious when BM3D is applied on the Mandril image in Figure 6, which is consistent with Table 1 that BM3D performs consistently poorly on the Mandril image. Figure 7 shows the denoising results of the Cameraman and Penguin images with peak values of 255 and 155, respectively.

5. Conclusions. In this paper, we proposed a novel Poisson denoising approach based on the fractional-order TV regularization. Using the properties of the function space of bounded FOTV, we proved the existence and uniqueness of the solution to the proposed model. Based on the primal-dual, forward-backward splitting, and ADMM optimization methods, we proposed three numerical algorithms, each with guaranteed convergence. A variety of numerical experiments were performed

Test Image	Peak	Noisy	NPTool	NLPCA	BM3D	Proposed
Cameraman	55	20.63	27.81/0.87	27.36/0.85	28.80/0.89	28.15/0.87
	155	25.18	30.65/0.91	29.52/0.87	29.06/0.90	30.90/0.92
	255	27.38	32.06/0.93	30.58/0.91	29.45/0.90	32.31/0.94
Penguin	55	19.53	30.86/0.91	30.49/0.89	31.50/0.92	31.46/ 0.92
	155	24.01	33.34 /0.94	32.14/0.91	32.37/0.93	33.86/0.95
	255	26.74	34.27/0.95	33.21/0.93	32.69/0.93	34.73/0.96
Train	55	20.94	28.04/0.88	27.20/0.81	28.01/0.89	28.25/0.88
	155	25.47	30.99 /0.92	29.64/0.88	28.31/0.89	31.06/0.92
	255	27.85	32.38/0.94	30.76/0.88	29.16/0.90	32.43/0.94
Mandrill	55	19.75	22.57/0.76	22.00 /0.71	20.39/0.56	22.80/0.76
	155	24.26	25.73/0.86	25.06/0.84	20.58/0.58	26.00/0.87
	255	26.46	27.67/0.90	26.46/0.87	20.95/0.60	27.76/0.91
Barbara	55	20.57	25.48/0.81	27.97/0.86	29.44/0.91	25.87/0.81
	155	25.14	28.52/0.87	30.29/0.90	30.77/0.93	29.14/0.89
	255	27.31	30.14/0.91	31.01/0.92	31.47/0.94	30.78/0.92

TABLE 1. Poisson denoising comparison. Each entry contains PSNR and SSIM values. The best results are highlighted in bold.

Test image (size)	Peak	NPTool	NLPCA	BM3D	Proposed
Barbara (512×512)	55	5.68	72.73	2.26	8.68
Train (512×357)	155	5.49	91.70	1.63	6.36
Mandrill (256×256)	255	1.99	3.77	0.71	1.32

TABLE 2. Computation time (in sec).

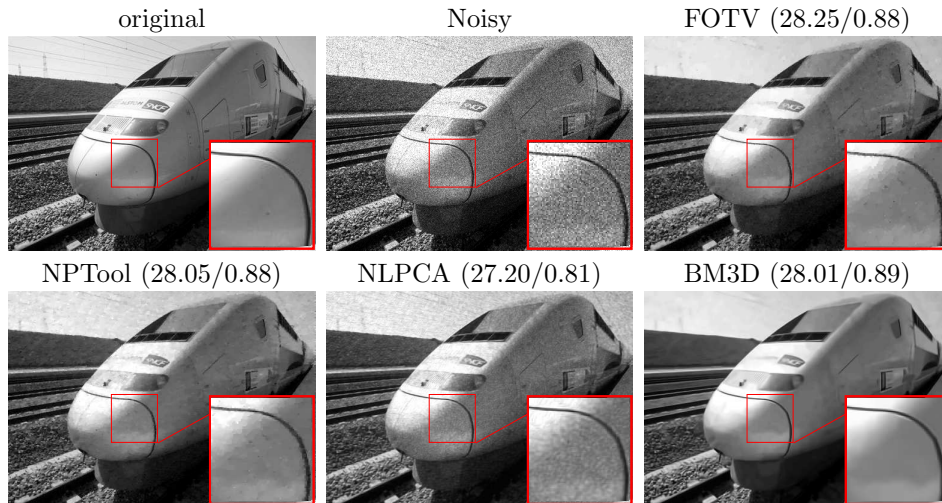


FIGURE 4. Poisson denoising results of Train image with peak at 55.

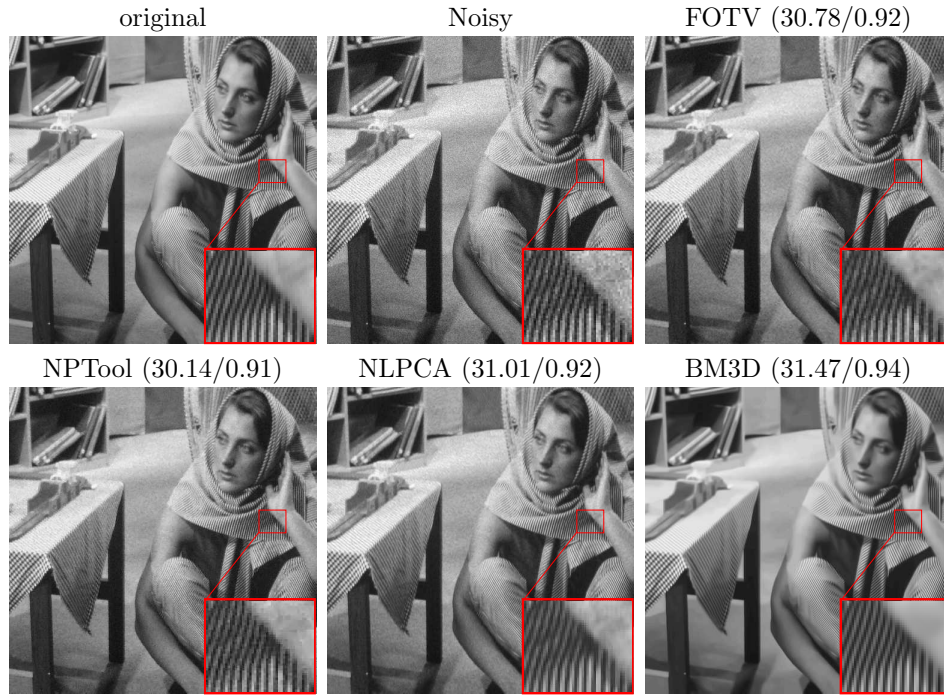


FIGURE 5. Poisson denoising results of Barbara image with peak at 255.

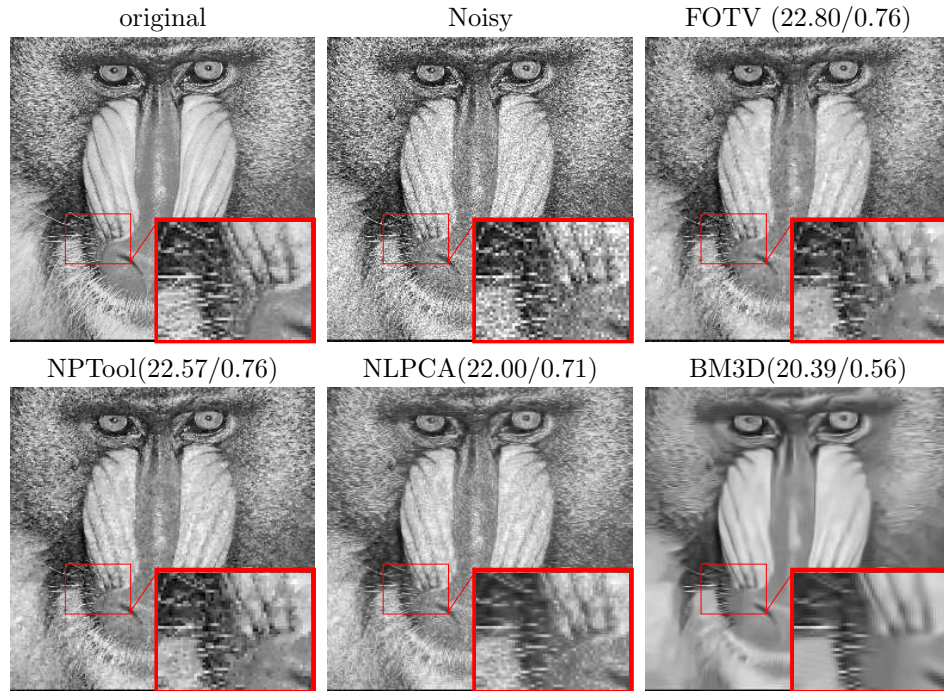


FIGURE 6. Poisson denoising results of Mandril image with peak at 55.

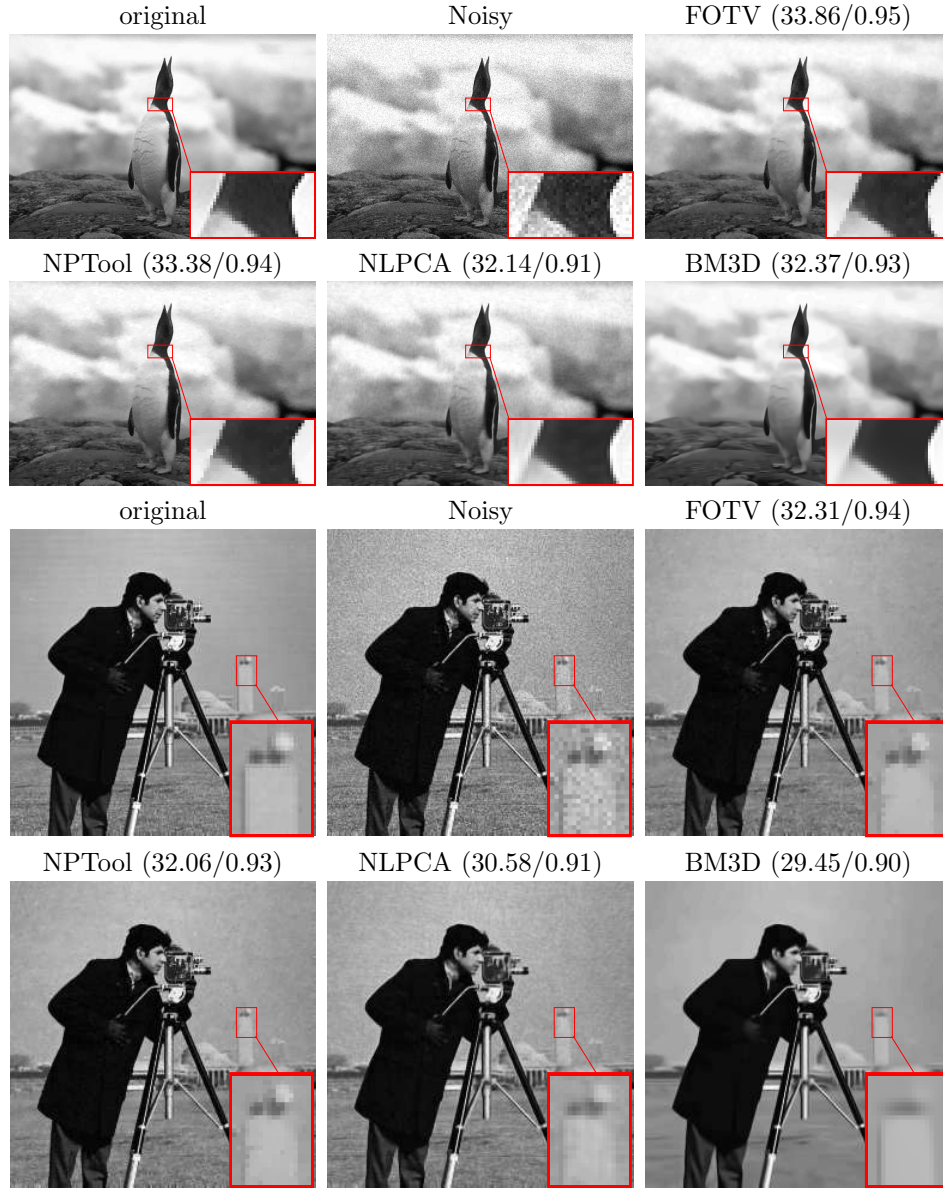


FIGURE 7. Poisson denoising results of Penguin image with peak at 155 and Cameraman image with peak at 255.

to justify the effectiveness of the proposed approaches in Poisson denoising. In particular, we used a synthetic image to investigate the optimal order of FOTV both theoretically and numerically. Furthermore, we compared our method with the state-of-the-art in Poisson denoising by testing five natural images with various levels of Poisson noise. Experimental results demonstrated the superior performance of the proposed approach over other competing ones. In the future work, we will explore acceleration techniques to further reduce the cost of computing fractional-order derivatives while improving the restoration accuracy.

Acknowledgments. JZ is partially supported by the Science and Technology Project of Jiangxi Provincial Department of Education (GJJ171015), the Natural Science Foundation of Jiangxi Province (20192BAB211005) and the China Scholarship Council (201708360066). JQ is supported by the NSF grant DMS-1941197. YL acknowledges the NSF awards of DMS-1522786 and CAREER DMS-1846690.

REFERENCES

- [1] J. Bai and X. C. Feng, [Fractional-order anisotropic diffusion for image denoising](#), *IEEE Trans. Image Process.*, **16** (2007), 2492–2502.
- [2] S. Bonettini and V. Ruggiero, [An alternating extragradient method for total variation-based image restoration from Poisson data](#), *Inverse Problems*, **27** (2011), 26pp.
- [3] S. Boyd, N. Parikh, E. Chu, B. Peleato and J. Eckstein, [Distributed optimization and statistical learning via the alternating direction method of multipliers](#), *Found. Trends Mach. Learn.*, **3** (2011), 1–122.
- [4] K. Bredies, K. Kunisch and T. Pock, [Total generalized variation](#), *SIAM J. Imaging Sci.*, **3** (2010), 492–526.
- [5] A. Chambolle, [An algorithm for total variation minimization and applications](#), *J. Math. Imaging Vision*, **20** (2004), 89–97.
- [6] A. Chambolle and T. Pock, [A first-order primal-dual algorithm for convex problems with applications to imaging](#), *J. Math. Imaging Vision*, **40** (2011), 120–145.
- [7] R. Chan, A. Lanza, S. Morigi and F. Sgallari, [An adaptive strategy for the restoration of textured images using fractional order regularization](#), *Numer. Math. Theory Methods Appl.*, **6** (2013), 276–296.
- [8] T. Chan, A. Marquina and P. Mulet, [High-order total variation-based image restoration](#), *SIAM J. Sci. Comput.*, **22** (2000), 503–516.
- [9] H. Chang, Y. Lou, M. K. Ng and T. Zeng, [Phase retrieval from incomplete magnitude information via total variation regularization](#), *SIAM J. Sci. Comput.*, **38** (2016), A3672–A3695.
- [10] D. Chen, Y. Q. Chen and D. Xue, [Fractional-order total variation image denoising based on proximity algorithm](#), *Appl. Math. Comput.*, **257** (2015), 537–545.
- [11] H. Chen, J. Song and X. C. Tai, [A dual algorithm for minimization of the LLT model](#), *Adv. Comput. Math.*, **31** (2009), 115–130.
- [12] K. Dabov, A. Foi, V. Katkovnik and K. Egiazarian, [Image denoising by sparse 3D transform-domain collaborative filtering](#), *IEEE Trans. Image Process.*, **16** (2007), 2080–2095.
- [13] D. di Serafino, G. Landi and M. Viola, [ACQUIRE: An inexact iteratively reweighted norm approach for TV-based Poisson image restoration](#), *Appl. Math. Comput.*, **364** (2020), 23pp.
- [14] F. Dong and Y. Chen, [A fractional-order derivative based variational framework for image denoising](#), *Inverse Probl. Imaging*, **10** (2016), 27–50.
- [15] Y. Duan, Y. Wang and J. Hahn, [A fast augmented Lagrangian method for Euler’s elastica models](#), *Numer. Math. Theory Methods Appl.*, **6** (2013), 47–71.
- [16] J. Eckstein and D. Bertsekas, [On the Douglas-Rachford splitting method and the proximal point algorithm for maximal monotone operators](#), *Math. Programming*, **55** (1992), 293–318.
- [17] M. Figueiredo and J. Bioucas-Dias, [Restoration of Poissonian images using alternating direction optimization](#), *IEEE Trans. Image Process.*, **19** (2010), 3133–3145.
- [18] M. Figueiredo and J. M. Bioucas-Dias, [Deconvolution of Poissonian images using variable splitting and augmented Lagrangian optimization](#), preprint, [arXiv:math/0904.4868](#).
- [19] W. Guo, J. Qin and W. Yin, [A new detail-preserving regularization scheme](#), *SIAM J. Imaging Sci.*, **7** (2014), 1309–1334.
- [20] L. Jiang, J. Huang, X. G. Lv and J. Liu, [Alternating direction method for the high-order total variation-based Poisson noise removal problem](#), *Numer. Algorithms*, **69** (2015), 495–516.
- [21] S. H. Kayyar and P. Jidesh, [Non-local total variation regularization approach for image restoration under a Poisson degradation](#), *J. Modern Optics*, **65** (2018), 2231–2242.
- [22] G. Landi and E. L. Piccolomini, [NPTool: A MATLAB software for nonnegative image restoration with Newton projection methods](#), *Numer. Algorithms*, **62** (2013), 487–504.
- [23] H. Lantéri and C. Theys, [Restoration of astrophysical images: The case of Poisson data with additive Gaussian noise](#), *EURASIP J. Adv. Signal Process.*, **2005** (2005), 2500–2513.
- [24] T. Le, R. Chartrand and T. J. Asaki, [A variational approach to reconstructing images corrupted by Poisson noise](#), *J. Math. Imaging Vision*, **27** (2007), 257–263.

- [25] D. Li, X. Tian, Q. Jin and K. Hirasawa, [Adaptive fractional-order total variation image restoration with split Bregman iteration](#), *ISA Transactions*, **82** (2017), 210–222.
- [26] H. Li, J. Wang and H. Dou, [Second-order TGV model for Poisson noise image restoration](#), *SpringerPlus*, **5** (2016).
- [27] Y. Li, J. Qin, Y. Hsin, S. Osher and W. Liu, [s-SMOOTH: Sparsity and smoothness enhanced EEG brain tomography](#), *Frontiers Neurosci.*, **10** (2016).
- [28] Y. Li, J. Qin, S. Osher and W. Liu, [Graph fractional-order total variation EEG source reconstruction](#), 38th Annual International Conference of the IEEE Engineering in Medicine and Biology Society (EMBC), Orlando, FL, 2016, 101–104.
- [29] X. Liu, [Augmented Lagrangian method for total generalized variation based Poissonian image restoration](#), *Comput. Math. Appl.*, **71** (2016), 1694–1705.
- [30] X. Liu and L. Huang, [Total bounded variation-based Poissonian images recovery by split Bregman iteration](#), *Math. Methods Appl. Sci.*, **35** (2012), 520–529.
- [31] X. G. Lv, J. Lee and J. Liu, [Deblurring Poisson noisy images by total variation with overlapping group sparsity](#), *Appl. Math. Comput.*, **289** (2016), 132–148.
- [32] M. Lysaker, A. Lundervold and X. C. Tai, [Noise removal using fourth-order partial differential equation with applications to medical magnetic resonance images in space and time](#), *IEEE Trans. Image Process.*, **12** (2003), 1579–1590.
- [33] J. Ma and D. Gemechu, [Anisotropic total fractional order variation model in seismic data denoising](#), *World Academy of Science, Engineering and Technology, International J. Geological and Environmental Engineering*, **12** (2018), 40–44.
- [34] L. Ma, T. Zeng and G. Li, [Hybrid variational model for texture image restoration](#), *East Asian J. Appl. Math.*, **7** (2017), 629–642.
- [35] M. Makitalo and A. Foi, [Optimal inversion of the Anscombe transformation in low-count Poisson image denoising](#), *IEEE Trans. Image Process.*, **20** (2011), 99–109.
- [36] S. Osher, A. Solé and L. Vese, [Image decomposition and restoration using total variation minimization and the \$H^1\$](#) , *Multiscale Model. Simul.*, **1** (2003), 349–370.
- [37] Y. Pu, [Fractional calculus approach to texture of digital image](#), *Proc. 8th Int. Conf. Signal Process.*, Beijing, China, 2006, 1002–1006.
- [38] Y. Pu, [Fractional differential analysis for texture of digital image](#), *J. Alg. Comput. Tech.*, **1** (2007), 357–380.
- [39] Y. Pu, W. Wang, J. Zhou, Y. Wang and H. Jia, [Fractional differential approach to detecting textural features of digital image and its fractional differential filter implementation](#), *Sci. China Ser. F*, **51** (2008), 1319–1339.
- [40] J. Qin and W. Guo, [An efficient compressive sensing MR image reconstruction scheme](#), IEEE 10th International Symposium on Biomedical Imaging, San Francisco, CA, 2013, 306–309.
- [41] J. Qin, F. Liu, S. Wang and J. Rosenberger, [EEG source imaging based on spatial and temporal graph structures](#), Seventh International Conference on Image Processing Theory, Tools and Applications (IPTA), Montreal, Canada, 2017, 1–6.
- [42] J. Qin, T. Wu, Y. Li, W. Yin, S. Osher and W. Liu, [Accelerated high-resolution EEG source imaging](#), 8th International IEEE/EMBS Conference on Neural Engineering (NER), Shanghai, China, 2017, 1–4.
- [43] J. Qin, X. Yi and S. Weiss, [A novel fluorescence microscopy image deconvolution approach](#), IEEE 15th International Symposium on Biomedical Imaging, Washington DC, 2018, 441–444.
- [44] L. I. Rudin, S. Osher and E. Fatemi, [Nonlinear total variation based noise removal algorithms](#), *Phys. D*, **60** (1992), 259–268.
- [45] J. Salmon, Z. Harmany, C. A. Deledalle and R. Willett, [Poisson noise reduction with non-local PCA](#), *J. Math. Imaging Vision*, **48** (2014), 279–294.
- [46] A. Sawatzky, C. Brune, T. Kusters, F. Wubbeling and M. Burger, [EM-TV methods for inverse problems with Poisson noise](#), in *Level Set and PDE Based Reconstruction Methods in Imaging*, Lecture Notes in Math., 2090, Springer, Cham, 2013, 71–142.
- [47] A. Sawatzky, C. Brune, J. Muller and M. Burger, [Total variation processing of images with Poisson statistics](#), in *Computer Analysis of Images and Patterns*, Lecture Notes in Computer Science, 5702, Springer, Berlin, Heidelberg, 2009, 533–540.
- [48] S. Setzer, G. Steidl and T. Teuber, [Deblurring Poissonian images by split Bregman techniques](#), *J. Vis. Commun. Image*, **21** (2010), 193–199.
- [49] J. Shen, S. H. Kang and T. F. Chan, [Euler's elastica and curvature-based inpainting](#), *SIAM J. Appl. Math.*, **63** (2002), 564–592.

- [50] X. C. Tai, J. Hahn and G. J. Chung, [A fast algorithm for Euler's elastica model using augmented Lagrangian method](#), *SIAM J. Imaging Sci.*, **4** (2011), 313–344.
- [51] A. N. Tikhonov, A. Goncharsky, V. V. Stepanov and A. G. Yagola, [Numerical Methods for the Solution of Ill-Posed Problems](#), Mathematics and its Applications, 328, Kluwer Academic Publishers Group, Dordrecht, 1995.
- [52] A. Ullah, W. Chen and M. A. Khan, [Fracto-integer order total variation based multiplicative noise removal model](#), International Conference on Information Science and Technology (ICIST), Changsha, China, 2015, 160–165.
- [53] A. Ullah, W. Chen and M. A. Khan, [A new variational approach for restoring images with multiplicative noise](#), *Comput. Math. Appl.*, **71** (2016), 2034–2050.
- [54] Y. Vardi, L. A. Shepp and L. Kaufman, [A statistical model for positron emission tomography](#), *J. Amer. Statist. Assoc.*, **80** (1985), 8–37.
- [55] X. D. Wang, X. C. Feng, W. Wang and W. J. Zhang, [Iterative reweighted total generalized variation based Poisson noise removal model](#), *Appl. Math. Comput.*, **223** (2013), 264–277.
- [56] Y. Wang, J. Yang, W. Yin and Y. Zhang, [A new alternating minimization algorithm for total variation image reconstruction](#), *SIAM J. Imaging Sci.*, **1** (2008), 248–272.
- [57] Z. Wang, A. C. Bovik, H. R. Sheikh and E. P. Simoncelli, [Image quality assessment: From error visibility to structural similarity](#), *IEEE Trans. Image Process.*, **13** (2004), 600–612.
- [58] Y. Wen, R. Chan and T. Zeng, [Primal-dual algorithms for total variation based image restoration under Poisson noise](#), *Sci. China Math.*, **59** (2016), 141–160.
- [59] C. Wu and X. C. Tai, [Augmented Lagrangian method, dual methods, and split Bregman iteration for ROF, vectorial TV, and high order models](#), *SIAM J. Imaging Sci.*, **3** (2010), 300–339.
- [60] J. Zhang and K. Chen, [A total fractional-order variation model for image restoration with nonhomogeneous boundary conditions and its numerical solution](#), *SIAM J. Imaging Sci.*, **8** (2015), 2487–2518.
- [61] J. Zhang, R. Chen, C. Deng and S. Wang, [Fast linearized augmented Lagrangian method for Euler's elastica model](#), *Numer. Math. Theory Methods Appl.*, **10** (2017), 98–115.
- [62] J. Zhang, M. Ma, Z. Wu and C. Deng, [High-order total bounded variation model and its fast algorithm for Poissonian image restoration](#), *Math. Probl. Eng.*, **2019**, 11pp.
- [63] J. Zhang, Z. Wei and L. Xiao, [Adaptive fractional-order multi-scale method for image denoising](#), *J. Math. Imaging Vision*, **43** (2012), 39–49.
- [64] J. Zhang, Z. Wei and L. Xiao, [A fast adaptive reweighted residual-feedback iterative algorithm for fractional-order total variation regularized multiplicative noise removal of partly-textured images](#), *Signal Process.*, **98** (2014), 381–395.
- [65] J. Zhang, Z. Wei and L. Xiao, [Bi-component decomposition based hybrid regularization method for partly-textured CS-MR image reconstruction](#), *Signal Process.*, **128** (2016), 274–290.
- [66] X. Zhang, M. K. Ng and M. Bai, [A fast algorithm for deconvolution and Poisson noise removal](#), *J. Sci. Comput.*, **75** (2018), 1535–1554.
- [67] W. Zhou and O. Li, [Poisson noise removal scheme based on fourth-order PDE by alternating minimization algorithm](#), *Abstr. Appl. Anal.*, **2012** (2012), 14pp.
- [68] W. Zhou and Q. Li, [Adaptive total variation regularization based scheme for Poisson noise removal](#), *Math. Methods Appl. Sci.*, **36** (2013), 290–299.
- [69] W. Zhu and T. Chan, [Image denoising using mean curvature of image surface](#), *SIAM J. Imaging Sci.*, **5** (2012), 1–32.

Received March 2019; revised August 2019.

E-mail address: mujib.chowdhury@utdallas.edu

E-mail address: junzhang0805@126.com

E-mail address: jing.qin@uky.edu

E-mail address: yifei.lou@utdallas.edu